Response of Extreme Precipitating Cell Structures to Atmospheric Warming

Kai Lochbihler[1,2] (ID), **Geert Lenderink[1]** (ID), and **A. Pier Siebesma[1,2]**

[1]The Royal Netherlands Meteorological Institute (KNMI), De Bilt, Netherlands, [2]Geoscience & Remote Sensing, Delft University of Technology, Delft, Netherlands

Abstract With increasing temperatures, it is likely that precipitation extremes increase as well. While, on larger spatial and longer temporal scales, the amplification of rainfall extremes often follows the Clausius-Clapeyron relation, it has been shown that local short-term convective precipitation extremes may well exceed the Clausius-Clapeyron rate of around 6.5%/K. Most studies on this topic have focused exclusively on the intensity aspect, while only few have examined (with contradictory results) how warmer and moister conditions modulate the spatial characteristics of convective precipitation extremes and how these connect to increased intensities. Here we study this relation by using a large eddy simulation model. We simulate one diurnal cycle of heavy convective precipitation activity based on a realistic observation-based strongly forced case setup. Systematically perturbed initial conditions of temperature and specific humidity enable an examination of the response of intensities and spatial characteristics of the precipitation field over an 8° dew point temperature range. We find that warmer and moister conditions result in an overall increase of both intensities and spatial extent of individual rain cells. Colder conditions favor the development of many but smaller rain cells. Under warmer conditions, we find a reduced number of individual cells, but their size significantly grows along with an increase of intensities over a large part of a rain cell. Combined, these factors lead to larger and more intense rain cells that can produce up to almost 20% more rain per degree warming and therefore have a large impact.

1. Introduction

How do the characteristics of rainfall extremes change with a warming atmosphere? This question has multiple dimensions and can be tackled from different angles.

The most obvious aspect is the intensity. Usually and already for several decades (Fischer & Knutti, 2016), changes in the intensity of rainfall extremes have been attributed to the increase in the water holding capacity of the atmosphere, as dictated by the Clausius-Clapeyron (CC) relation. Indeed, a number of global modeling studies have confirmed that changes in daily precipitation extremes scale with the CC rate—7%/K—when aggregated over large areas (Allen & Ingram, 2002; Pall et al., 2007; Tebaldi et al., 2006), although substantial deviations have been observed over the tropical and subtropical oceans due to large-scale dynamical feedbacks (Pfahl et al., 2017). At the other end of the spectrum of precipitation extremes, at small spatial and temporal scales, the CC relation is also playing a key role in understanding its behavior in response to warming. Station observations show that hourly and subhourly precipitation extremes can display dependencies on surface (dew point) temperature up to two times the CC relation (Lenderink & van Meijgaard, 2008; Lenderink et al., 2011; Loriaux et al., 2013; Mishra et al., 2012). This enhanced CC scaling of local short-term rainfall extremes can be largely attributed to convective precipitation events (Berg et al., 2013; Moseley et al., 2013). A common hypothesis is that amplified latent heat release through higher temperatures and moister conditions leads to increased buoyancy and hence to more vigorous convective updrafts (Trenberth et al., 2003). This potentially leads to stronger moisture fluxes into convective updrafts at the cloud base but also laterally from the cloud environment (Loriaux et al., 2013; Lenderink et al., 2017; Singleton & Toumi, 2013). Recent research shows that the sub-cloud moisture convergence increases with surface temperature in convection resolving model simulations of extreme convective precipitation (Haerter et al., 2017; Moseley et al., 2016). And even more, the spatial extent of these areas of moisture divergence and convergence increases with temperature. Therefore, this provides evidence that convective events collect moisture from larger areas with increasing temperature and moisture availability.

Thinking straightforwardly, this could imply that the spatial properties of the precipitation footprint of convective events vary with temperature and moisture availability. However, there are few studies dedicated to this aspect, and the results are contradictory. Wasko et al. (2016), for instance, show that storms in Australia become more concentrated to the center and smaller in spatial extent. A similar analysis by Li et al. (2018) based on station observations and regional climate models arrives at the same conclusion. By analyzing rain radar data covering an eastern Mediterranean region, Peleg et al. (2018) also found increases in the intensity at the center of the convective cells with surface temperature but unchanged to small decreases in the area of convective cells. So all of these studies point at a redistribution of rain intensity toward the center of the convective cell at the expense of the spatial extent. However, in contrast to these findings, Lochbihler et al. (2017) find that convective cells grow in size at higher dew point temperatures and that this growth accelerates beyond 17 to 18 °C dew point temperature. For the same region, Lenderink et al. (2017) obtain from station records of hourly precipitation that rainfall events at higher dew point temperatures blanket more stations than at lower dew point temperatures. In addition, a recent modeling study with a convective permitting model showed a largely increased rain volume for the most intense convective systems that mainly resulted from an increase in spatial extent (Prein et al., 2017).

These contradictory findings show that the precise mechanisms of how warming influences the properties of convective rain cells remain still highly uncertain. There is reasonable consensus that intensities of convective rainfall events increase at a rate close to or beyond the CC rate (Westra et al., 2014). However, whether convective rain cells respond at a rate close to twice the CC rate, as suggested by surface observations in a number of regions, is still unclear. As an aside, we note here that part of the contradictory results may well be related to the fact that some of these studies use dew point temperature, a direct measure of near surface absolute humidity, whereas it is still more common to use temperature as the scaling variable (Lenderink et al., 2018; Wasko et al., 2018). For the spatial aspects, results are even more unclear, and both reductions in spatial extent with (dew point) temperature as well as increases are reported.

Therefore, we will here study these characteristics in idealized experiments using a high-resolution large eddy simulation (LES) model. In particular, we aim to answer the following questions: (i) How does precipitation intensity and area respond to warming, (ii) what is the relation between intensity and cloud rain cell size, and (iii) are there indications of a redistribution of cell intensities toward the center at the expense of cell size or rain intensities at the rain cell borders.

More specifically, we conduct simulations of a diurnal cycle with typical conditions for heavy convective precipitation in the Netherlands. This case setup is characterized by substantial time varying forcing from the surface as well as the large-scale circulation which forces the system out of equilibrium (Loriaux et al., 2017). Therefore, our simulations are fundamentally different from quasi-equilibrium simulations performed, for instance, for the tropics, in radiative-convective equilibrium (e.g., Muller et al., 2011; Romps, 2011). By systematically varying the initial state of temperature and humidity, we investigate the temporal evolution of surface precipitation and the response of the rainfall field to increasing temperatures and humidity in a range from 12 to 18 °C dew point.

2. Methods
2.1. LES Setup
Simulations are carried out using the Dutch Atmospheric LES (DALES) model (version 4.1; Böing et al., 2012; Heus et al., 2010). DALES is a LES model which uses the anelastic approximation with a turbulent kinetic energy equation for subgrid transports. The source code is distributed under the GNU General Public License v3.0 and available online (https://github.com/dalesteam/dales). A single-moment cloud microphysics scheme (Böing et al., 2012; Grabowski, 1998) is used, and the radiative cooling and surface fluxes (supporting information Figure S1) are prescribed. For a full description of the model equations, we refer to the above-mentioned publications and the source code repository. The complete model setup is available from Data Set S1.

The experimental setup follows the approach developed in Loriaux et al. (2017), specifically designed to produce a simple but yet realistic forcing for convective situations. Based on a catalog of rainfall events in the Netherlands from the past 20 years (Lenderink et al., 2017), we create a composite of approximately 300 days with heavy hourly precipitation in the summer season (April to September) in the afternoon hours (1200 to 2000 CET). Our selection is further constrained to the top 20% most intense events at dew point
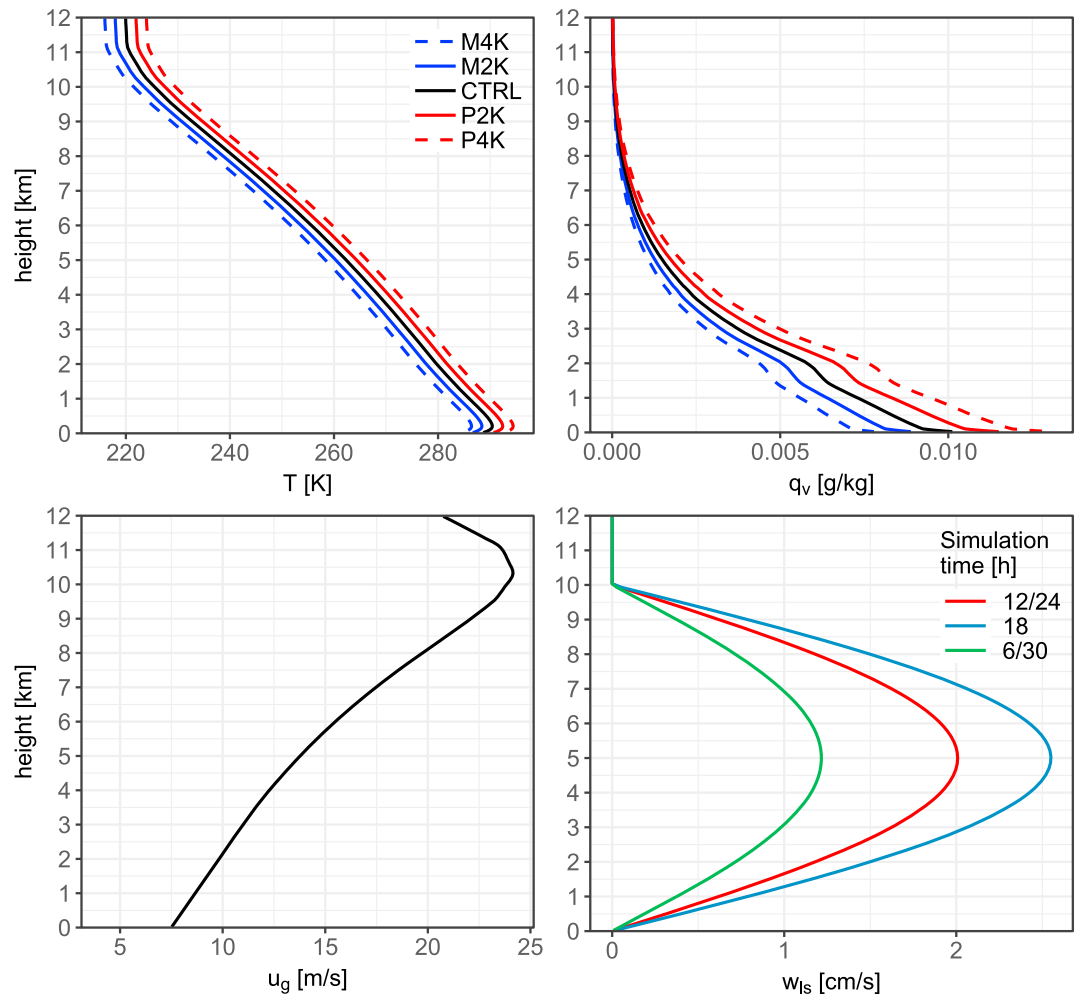
Figure 1. Initial profiles for temperature T and water vapor specific humidity q_v. The geostrophic wind forcing u_g is the same for all experiments and constant in time. The idealized large-scale vertical velocity w_{ls} varies in time but is symmetric to the time step at 18 hr of simulation. Here, vertical profiles of w_{ls} are shown for 6 (30), 12 (24), and 18 hr of simulation. For a time-height plot of w_{ls}, see Figure S2.

temperatures above 14 °C. Detailed statistics of the event catalog can be found in Table 1 of Lenderink et al. (2017). On average, these events take place at a surface dew point temperature of 16 °C and have a peak intensity of 15 mm/hr.

As in Loriaux et al. (2017), we retrieved the necessary data for the initialization, the large-scale forcing, and the surface fluxes from a concatenation of hindcasts of the regional climate model RACMO (Meijgaard et al., 2012) at a resolution of 12 km, initialized, and forced with ERA-interim reanalysis data (Dee et al., 2011).

Initial profiles of temperature and humidity (Figure 1) are a composite of the 0400 CET conditions at the station with the highest rainfall amounts of each event. The model is forced with time variable (0400 to 0400 CET of the following day) surface sensible and latent heat fluxes (see Figure S1). In this case, the averaging was done over all stations within a radius of 70 km around the event location. Furthermore, a geostrophic wind profile (Figure 1) is calculated in a similar manner as the surface fluxes. Because the derived geostrophic wind profile has only little temporal variability, we applied it as a constant forcing in time to DALES. We calculated the wind speed from u and v components before averaging and serve it to DALES as the u component only.

Most extreme convective events in the Netherlands occur with considerable synoptic-scale convergence, inducing a large-scale upward vertical velocity (omega) that humidifies and destabilizes the atmosphere (Lenderink et al., 2017; Loriaux et al., 2017). This forcing is imposed in DALES through a large-scale vertical

velocity (Loriaux et al., 2017) and varies in time and with height as shown in Figure S2. The lower right panel in Figure 1 shows the omega forcing (w_{ls}) at three example time steps of the simulation. In contrast to Loriaux et al. (2017), the resulting average omega field from the selection of cases has been idealized. This has been done to filter out noise in time and height which would complicate the analysis of the results (see Lenderink et al., 2017; Loriaux et al., 2017, for some typical results of these averaged omega fields for a typical selection of events).

Based on the control (CTRL) run, we simulate four additional experiments with perturbed initial conditions. The initial profile for temperature is increased/decreased uniformly in steps of 2 K. Keeping relative humidity constant, which is (to first order) representative in the context of climate change (Attema et al., 2014), results in an increase/decrease of the initial specific humidity profile. We term these perturbed simulations M4K (−4 K), M2K (−2 K), P2K (+2 K), and P4K (+4 K), according to the temperature deviation relative to the control simulation.

Simulations are carried out on a domain with an extent of 192 km × 192 km in the horizontal directions and approximately 21 km in the vertical dimension. A sponge layer is used at levels above 13 km which is well beyond the maximum cloud top height. A horizontal grid spacing of 200 m makes 960 × 960 grid points. The vertical grid, 240 levels, is nonequidistant with a level thickness of around 40 m near the surface and up to 150 m in the highest model levels. To provide ample time for convective organization, we stretch out the simulation day by a factor of 1.5 (Haerter et al., 2017; Moseley et al., 2016). This decision is motivated by two aspects. First, the model is initiated with a nearly homogeneous atmosphere in horizontal directions and turbulence needs time to build up (spin-up) during the first hours of simulation. This delays the organization of convection, and testing has shown that the highest precipitation rates are reached way beyond the peak of the large-scale forcing in the normal day setup. By giving the system more time to organize, the timing of the highest precipitation rates shifts toward the peak of the large-scale convergence and surface forcing, which is closer to observed cases (Lenderink et al., 2017). The second aspect is that this approach increases the data output and enables more robust statistics at a reasonable additional computational cost. We stop the simulations after 30 hours since we are interested in the daytime part where the large-scale forcings are the strongest.

2.2. Precipitation Statistics and Rain Cell Clustering

The simulations produce output of surface precipitation at a time step of 1 min with the full horizontal resolution. To reduce the data amount and to ease the rain cell clustering later on, we coarse-grain the data to a grid spacing of 400 m. This also drastically reduces the number of very small rain cells with low intensities. We also apply a minimum threshold of 0.6 mm/hr. Smaller values are set to zero. In the remainder of this study, we will use the following notation, which is, for means of simplicity, given here for a single time step.

We define the total area with surface precipitation exceeding the threshold as A. The nondimensional area fraction with rain is

$$a = A/A_D, \tag{1}$$

where A_D is area of the full domain (192 × 192 km). Note that we use the lower case letters for nondimensional quantities. The total rain rate over the domain—called rain yield hereafter and denoted by P—is the rain rate aggregated over the domain and normalized by A_D. We also consider the rain rate P_r conditional on the precipitation area. They are trivially related by

$$P = aP_r. \tag{2}$$

At each time step, the surface precipitation output is clustered to continuous areas with rain, from now on referred to as rain cells. The algorithm to cluster is identical to Lochbihler et al. (2017). Accordingly, neighboring grid points with precipitation above the threshold belong to the same cell. Diagonal adjacency is not allowed. The number of cells is given by N. Each cell i has different properties given by its size A_i and its mean intensity $P_{i,r}$, which is the sum of the rain rates over all grid points divided by the number of grid points belonging to the cell. The linear size L_i of a cell is defined as the linear length given by the square root of the cell area

$$L_i = \sqrt{A_i}. \tag{3}$$

Whenever we use the term size of a cell, we refer to this linear length.

We also define the cell-aggregated rain rate, which is given by

$$P_{i,\mathrm{car}} \equiv A_i P_{i,r} = L_i^2 P_{i,r}, \tag{4}$$

which is just the total rain produced by a cell per time unit. From an impact point of view, this cell-aggregated rain rate is important when integrated over the life time of a cell as it quantifies the total amount of rain produced by a rain cell. Also, it is dynamically important as it relates to the net rate of latent heat release produced by the cell.

The domain-averaged rain yield and rain rate can be expressed in terms of the cell statistics as

$$P = \frac{\sum_{i=1}^{N} A_i P_{i,r}}{A_D}, \tag{5}$$

$$P_r = \frac{\sum_{i=1}^{N} A_i P_{i,r}}{A}, \tag{6}$$

where A is simply the sum of the area of all cells

$$A = \sum_{i=1}^{N} A_i, \tag{7}$$

so that the rain rate P_r is the cell-area-weighted mean of the individual cell rain rates $P_{i,r}$.

Besides the statistics of all rain cells, we also investigate the statistical properties of cells of a certain size or exceeding a certain size. In that case, the number of cells does not equal the total number of cells N but is constrained to a subset of cells satisfying a condition for L_i. For instance, a conditional precipitation rate $P_{L_1-L_2,r}$ for cells with a size between L_1 and L_2 is computed from

$$P_{L_1-L_2,r} = \frac{\sum_{i=1}^{N} I_{L_1-L_2}(i) P_{i,r}}{\sum_{i=1}^{N} I_{L_1-L_2}(i)}, \tag{8}$$

where the indicator function $I_{L_1-L_2}(i)$ has been introduced and is defined as

$$\begin{aligned} I_{L_1-L_2}(i) &= 1 \text{ if } \quad L_1 < L_i \quad \leq L_2 \\ &= 0 \text{ otherwise.} \end{aligned} \tag{9}$$

3. Results

3.1. Temporal Evolution of Surface Precipitation

Figure 2 shows time series of the precipitation area fraction a, the precipitation yield P, and the precipitation rate P_r. All experiments show a similar temporal evolution for all quantities. However, we first focus on the CTRL run to illustrate the interplay between these different measures.

After the onset of rainfall, at hour 11, the area fraction rapidly increases and peaks approximately one and a half hours later. During the following one and a half hours, the area fraction drops by more than a half to about 6 % and, with a slight relief, remains at this level for about 4 hr. Following this, it reaches an even lower level for the remainder of the simulation.

A similarly phased evolution is visible in the time series of precipitation yield but with even sharper transitions from lower to higher values. The precipitation yield reaches a first maximum value around hour 12 and a second peak 5 hr later. In between, there is a period of 2 hr with less activity. The area fraction considerably differs between these two time windows. This indicates that the precipitation field as a whole undergoes significant changes.

At this point we introduce the definition of two phases of precipitation activity with distinct spatial characteristics as well as intensities (gray areas in Figure 2). We note that these two phases are by no means discrete stages of the simulation but rather part of a continuous transformation of precipitation characteristics. By choosing time intervals of the same length, we obtain two comparable samples to robustly probe the precipitation field at different stages during the process of convective organization. Phase I is the time frame
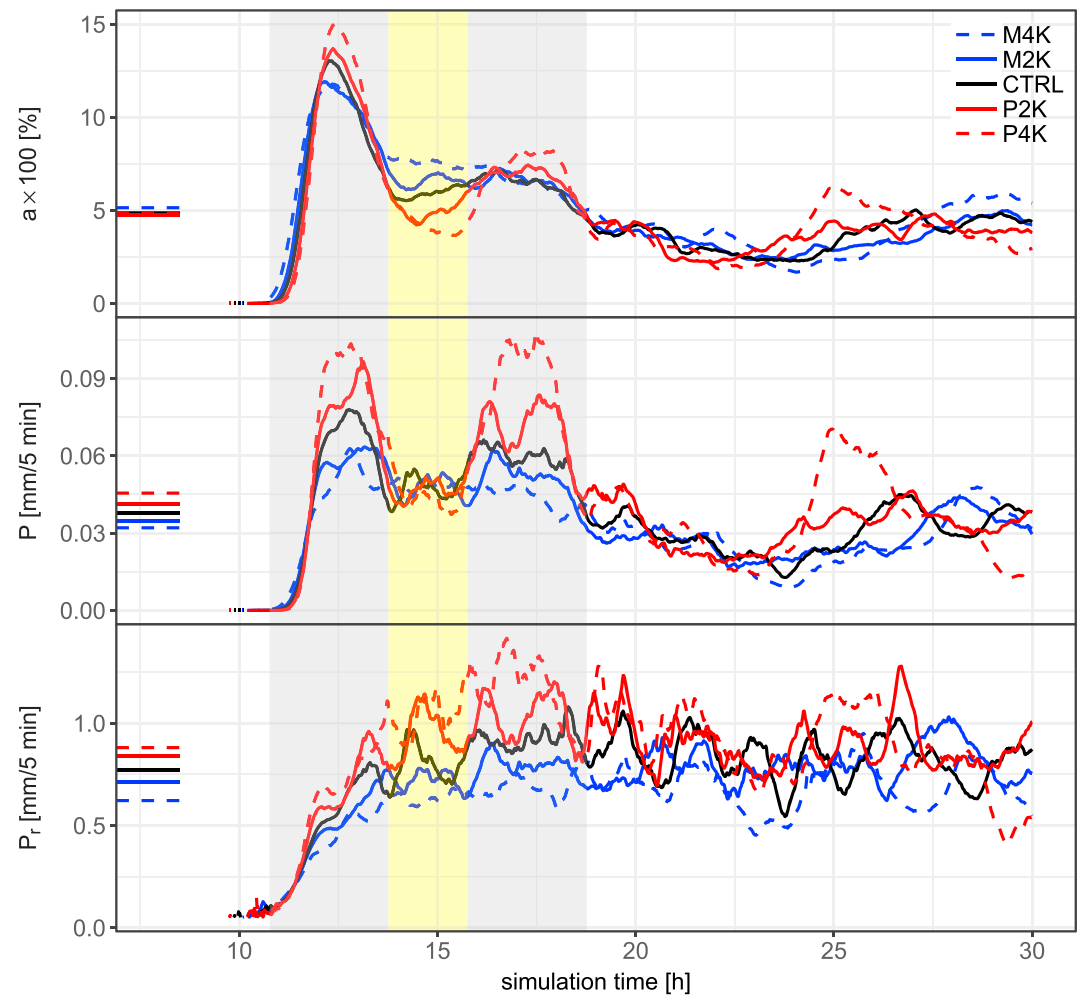
Figure 2. Time series of domain-averaged precipitation measures for all experiments. (from top to bottom) The precipitation area fraction a, the precipitation yield P, and the precipitation rate P_r. The gray areas mark the selected time frames for phases I and II (see text for explanation). The yellow area is the transition phase. The line segments on the y axis mark the time average of each quantity.

around the first peak of area fraction. This phase is also characterized by a sequence of relatively high values of precipitation yield. In a similar way, we define phase II as the time window which covers the second plateau of precipitation yield. Both phases have a length of 3 hr and cover the two peaks of the precipitation yield. We call the time span between the two phases the transition phase (yellow area in Figure 2).

The area fraction in phase II is considerably lower than in phase I. Since the level of precipitation yield in phase II is comparable to phase I, the precipitation rate must compensate this. Indeed, the precipitation rate continuously increases roughly until the end of phase II. Afterward, the precipitation rate shows no clear tendency but larger fluctuations than before. Thus, the precipitation field in phase I is characterized by a relatively large precipitation area with relatively low rainfall intensities. During the transition to phase II, the precipitation area decreases, but the rain rate increases.

The temporal evolution of all three precipitation characteristics is similar for all experiments, but there are also substantial differences. The area fraction in phase I peaks at higher values in the warmer runs. In contrast to that, the area fraction in the transition phase is higher for colder experiments. All runs reach approximately the same area fraction in phase II. The precipitation yield shows a similar systematic behavior. From the coldest to the warmest experiment, the yield gradually increases in both phases. The precipitation rate correspondingly increases until the end of phase II in all experiments with the highest/lowest values in the P4K/M4K run.
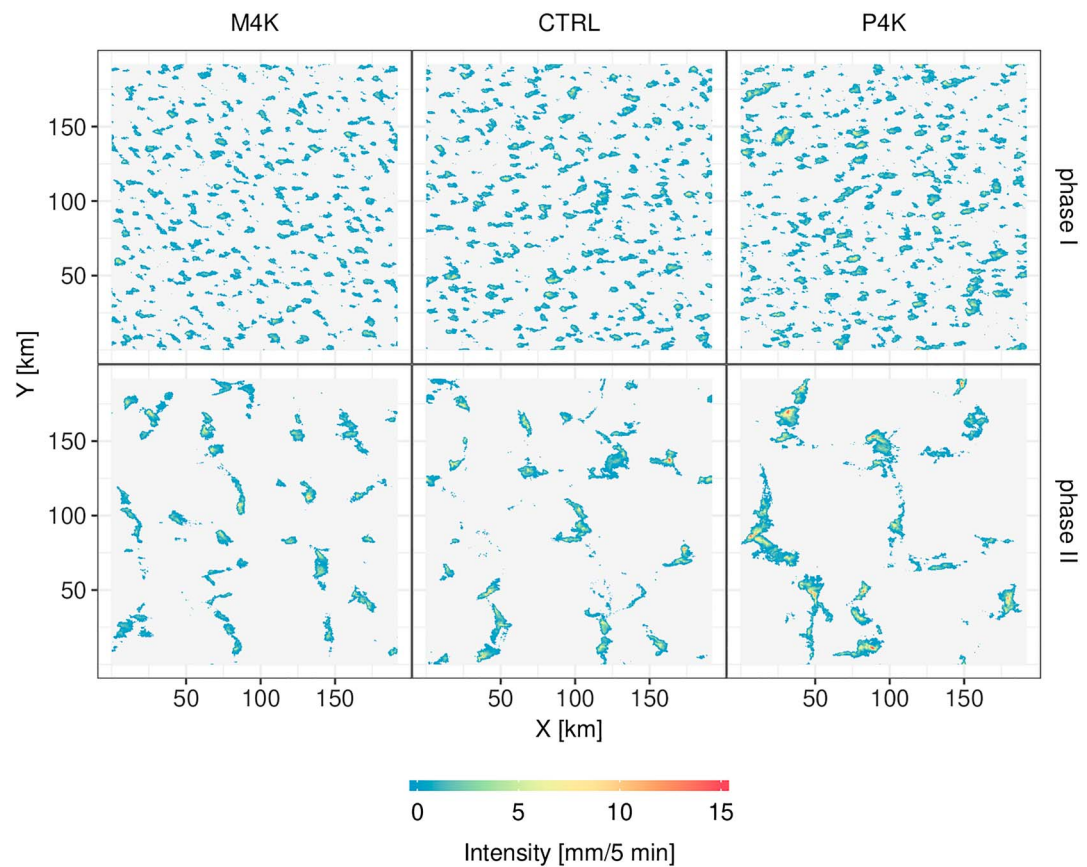
Figure 3. Snapshots of the precipitation field at the center of phases I and II (upper and lower panels). Three experiments: M4K, CTRL, and P4K (left to right). Gray areas indicate no or below-threshold precipitation.

There are two major characteristics which deserve additional attention in this context. First, the timing of the two phases is nearly the same across all experiments. This is aided by the fact that we used perturbations in temperature while keeping the relative humidity constant, which implies an unchanged dew point depression and therefore approximately the same lifting level of condensation. Moreover, all experiments share the same prescribed large-scale forcing for convergence and surface fluxes (see Figures S2 and S1). Consequently, the destabilization of the atmosphere and initiation of convection as well as the point where saturation and finally precipitation sets in are similarly timed between the experiments. The same factors play a crucial role for the timing of phase II. Due to the moisture removal through rain in phase I, it takes time until the surface latent heat flux and moisture input through large-scale convergence (which scales roughly with the CC relation; see Figure S3) replenish this deficit. Simultaneously, the surface heat flux and large-scale convergence counteracts the stabilizing effect of convection from phase I: While the surface forcing causes a warming in the lower levels, the large-scale convergence which is strongest in the midtroposphere (see Figure S2) induces cooling (see Figure S4). This aspect is closely connected to the second peculiarity: the occurrence of the transition phase in between the two active phases. In warmer runs, we observe a higher precipitation area fraction, rate, and yield in phase I. Thus, the stabilizing effect is stronger (see Figure S4) and affects a larger part of the domain which then leads to a lower area fraction in the transition phase before phase II sets in.

Up to the end of phase II, at hour 18, convective activity shows a systematic response to the warmer and moister atmospheric conditions. These are imposed by the initial conditions but also by the dependency of the large-scale moisture convergence which roughly follows the CC relation (Loriaux et al., 2017). After phase II, the response is less systematic, and because of large temporal variations, it is also more difficult to compare the different runs. Part of this may be related to the fact that the surface forcing is small after 18 hr (see Figure S1), which limits further destabilization of the atmosphere. Further on, we will therefore focus
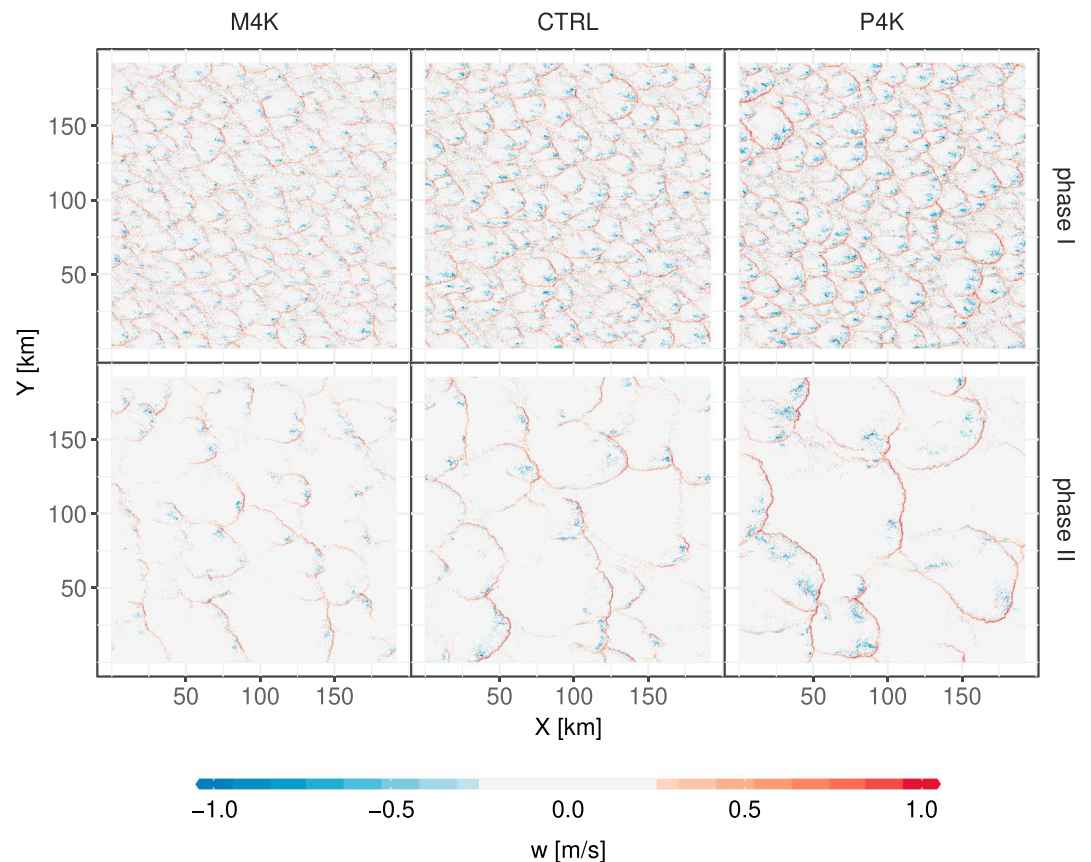
Figure 4. Snapshots of vertical velocity w at a height of 100 m. Note that values between -0.25 and $+0.25$ m/s are colored in gray.

on the two active phases I and II because they show a clearly systematic behavior and they are still relatively strongly influenced by the initial conditions and the large-scale forcing (Figures S1 and S2).

3.2. Spatial Characteristics of the Precipitation Field

A qualitative overview of how the spatial variability in the precipitation field depends on temperature and humidity can be achieved by looking at snapshots at different stages of the simulation. In Figure 3, we show the rainfall field at the center of the time windows of phases I and II for the M4K, CTRL, and P4K runs. Phase I is characterized by many, more or less regularly distributed rain cells of small spatial extent. Five hours later in phase II, most of the smaller rainfall areas have been replaced by or grown into considerably larger cells. Moreover, rain cells become larger and more intense under warmer and moister conditions in both phases.

The evolution from finer to coarser structures is similar to the results of Moseley et al. (2016) where the spatial scale of areas of low level moisture convergence and divergence increases in the course of the simulation. Indeed, a Hovmoeller diagram of vertical velocity, a proxy for convergence, at 100 m (Figure S5) reveals comparable patterns. Snapshots of the full horizontal field in phases I and II complement the picture, indicating that distances between regions of strong convergence increase (Figure 4). The process seems to be amplified by higher temperatures.

In the following sections, we will, according to the structure of Figure 3, examine how the spatial variability and intensities change with varying temperature, as well as between the two active phases of convective rainfall. To this purpose, we investigate the properties of rain cells, which are defined as continuous areas with rainfall. We extract the size L (square root of the area) of rain cells in phases I and II and calculate the number of cells that exceed a certain size (Figure 5). In phase I, all experiments have similar distributions up until a size threshold of approximately 5 km. Beyond this size, the distributions diverge for the different experiments. For instance, rain cells larger than 8 km are, in absolute terms, four times more frequent in
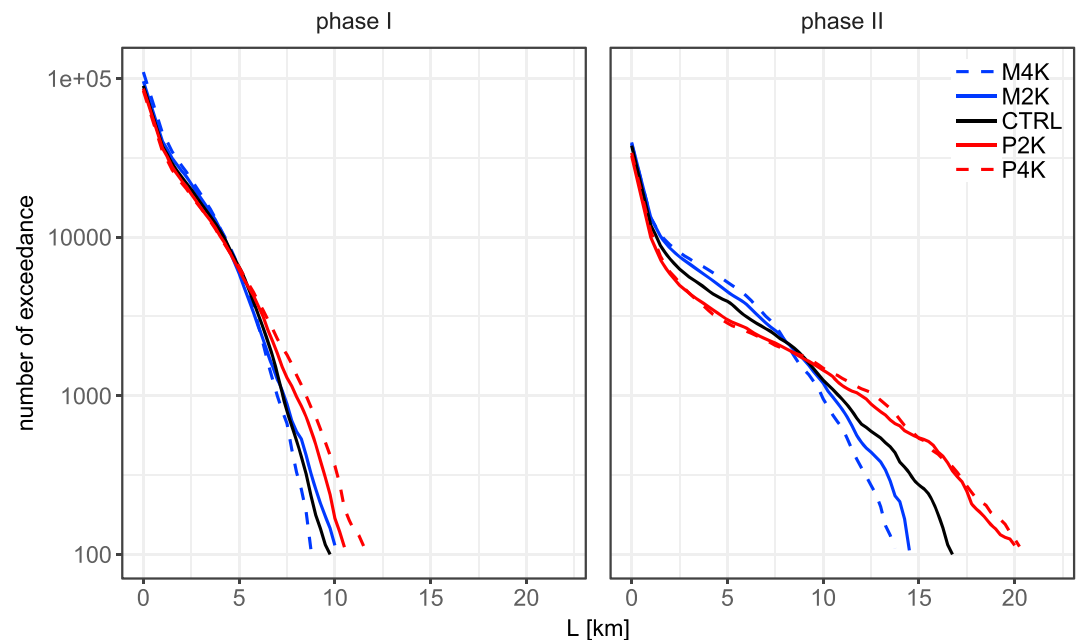
Figure 5. The number of rain cells which exceed a certain size L in phases I and II. We cut off at the threshold with less than 100 cells left. Note the logarithmic y axis.

the P4K run than in the M4K run. This represents a corresponding change of the empirical cumulative distribution function for the different experiments (Figure S6). Thus, larger rain cells grow further in size and become more frequent with increasing temperature and moisture availability.

Proceeding to phase II in Figure 5, we see a drastic change of the situation. A remarkable difference to phase I is the general increase of rain cell size. Across all experiments, the curves reach higher values before they drop off to very low numbers of cells. Another distinct difference to phase I is the weaker decrease of number of cells with cell size which implies that the total rainfall area is more determined by the larger cells. Again, a consultation of the empirical cumulative distribution function confirms the aforementioned aspects (see Figure S6). Colder runs bear a larger number but smaller sized rain cells than the warmer runs. The precipitation field of the warmer runs is characterized by fewer but larger rain cells. The total number of rain cells in each phase varies accordingly: In phase I, the P4K run has 24% less cells compared to the M4K run; in phase II, it is 12%. This characteristic is also visible in the top panel ($L > 0$) of Figure 6.

The temporal evolution of the transition from smaller to larger cells in the course of the simulation is depicted in Figure 6. Choosing a rain cell size of 9 km and counting the number of cells that exceed this value (within a moving time window of 1 hr) reveal a nearly continuous scale increase across all experiments. For the lower threshold (6 km), we see that warmer model runs have more cells in phase I than the colder experiments. In phase II, this hierarchy reverses. For the higher thresholds, a clear dominance of the warmer experiments emerges. A threshold of 12 km is already beyond the range of the cell size distribution of phase I for all experiments except P4K. None of the experiments reaches cell sizes exceeding 15 km. The presence of such cells kicks in during the transition to phase II with the strongest rate of increase in the P2K and P4K runs. However, about 2 to 3 hr after phase II, the time series of all experiments reach a comparable level, and the temporal variability is clearly larger than the systematic differences between the experiments. Snapshots of the precipitation field in this part of the simulation (Figure S7) show no clear tendency of an increase of rain cell size with dew point temperature. A replication of Figure 5 with data from two additional time windows, centered at 23 and 27 hr of simulation time (Figure S8), confirms the lack of a systematic response of rain cell sizes to the perturbed initial conditions in the last part of the simulation.

3.3. Rainfall Intensity and the Relation to Spatial Properties

Besides the growth of the largest rain cells with dew point temperature, the snapshots in Figure 3 indicate an accompanying intensification of rainfall rates. To quantify this relation, we perform a scaling analysis. More specifically, we relate extreme rainfall statistics to dew point temperature and calculate the fractional
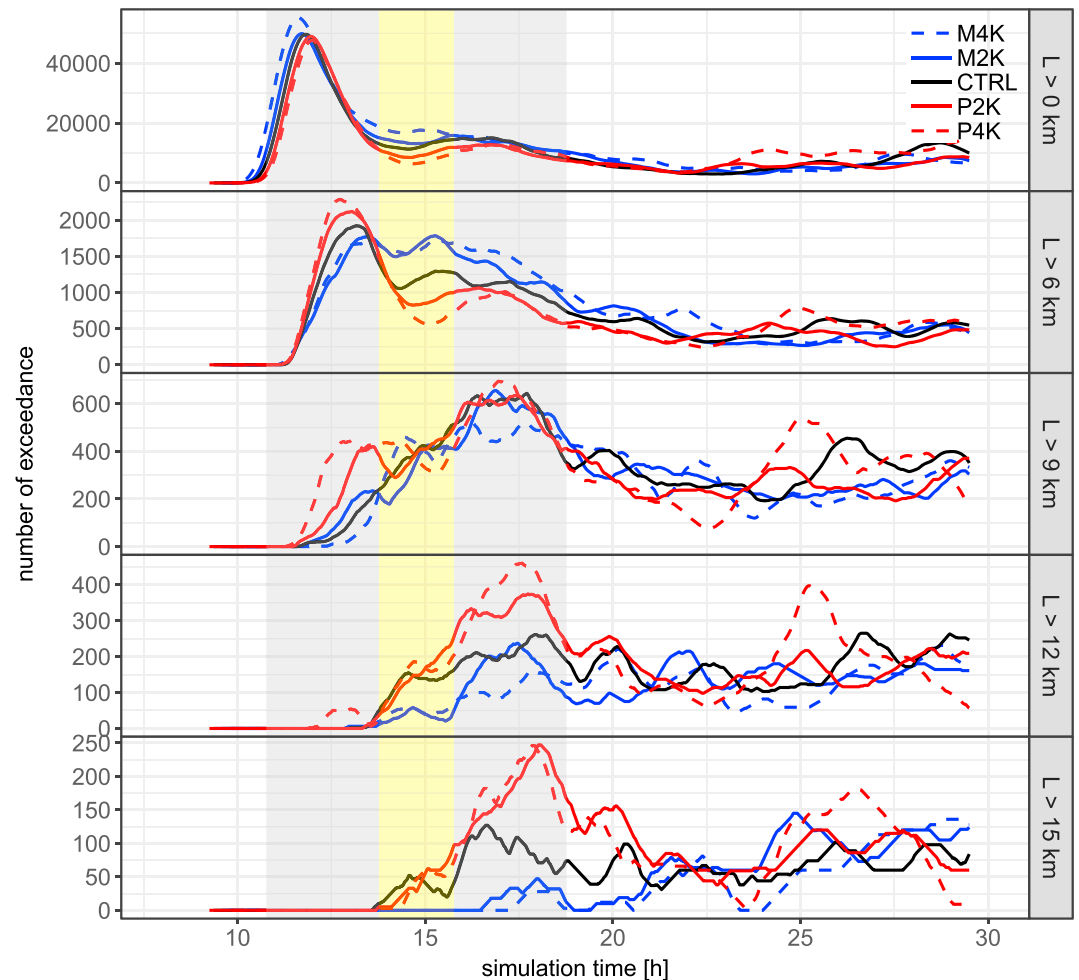
Figure 6. Time series of number of exceedance conditional on various thresholds for size L (gray box on the right side). Numbers are counted in a moving time window of 1 hr.

rate of change by fitting a linear model to log-transformed precipitation intensities. To obtain an overview on the general increase of intensities with dew point temperature, we first carry out the scaling analysis for unconditional grid point based rainfall rates. The most left panels in Figure 7 show the results for both phases. To ease the visual interpretation of the scaling rates, we transformed the y axis to a logarithmic scale and added auxiliary lines that indicate a fractional increase of 10%/K. Thus, the slope of the scaling line is the fractional rate of change per degree dew point temperature.

In correspondence to Figure 2, intensities are higher in phase II compared to phase I. Also, intensities are higher for the warmer runs. Depending on the chosen percentile, they scale with a rate ranging from around 7.8%/K to approximately 10%/K. Despite the difference in intensities between phases I and II, the scaling rates are quite similar.

To examine how this finding relates to the intensities of rain cells, we repeated the analysis with rain cell average intensities instead of grid point intensities. The results are depicted in the middle panels of Figure 7. Similar to the grid point intensities, the two highest percentiles of rain cell average intensities follow approximately the same scaling rate in both phases and are only shifted on the vertical axis. However, for the lower percentiles in phase II, scaling rates stall and even reverse to a negative scaling. Moreover, compared to the grid point based scaling estimate, we find that rain cell average intensities scale at lower rates ranging from 5.3%/K to 7.2%/K for the 97.5th and 99th percentiles.

Taking into account the rain-cell size, we repeated the analysis with the cell-aggregated rain rate. The right panels in Figure 7 show the results. The large difference in absolute values between phases I and II reflects
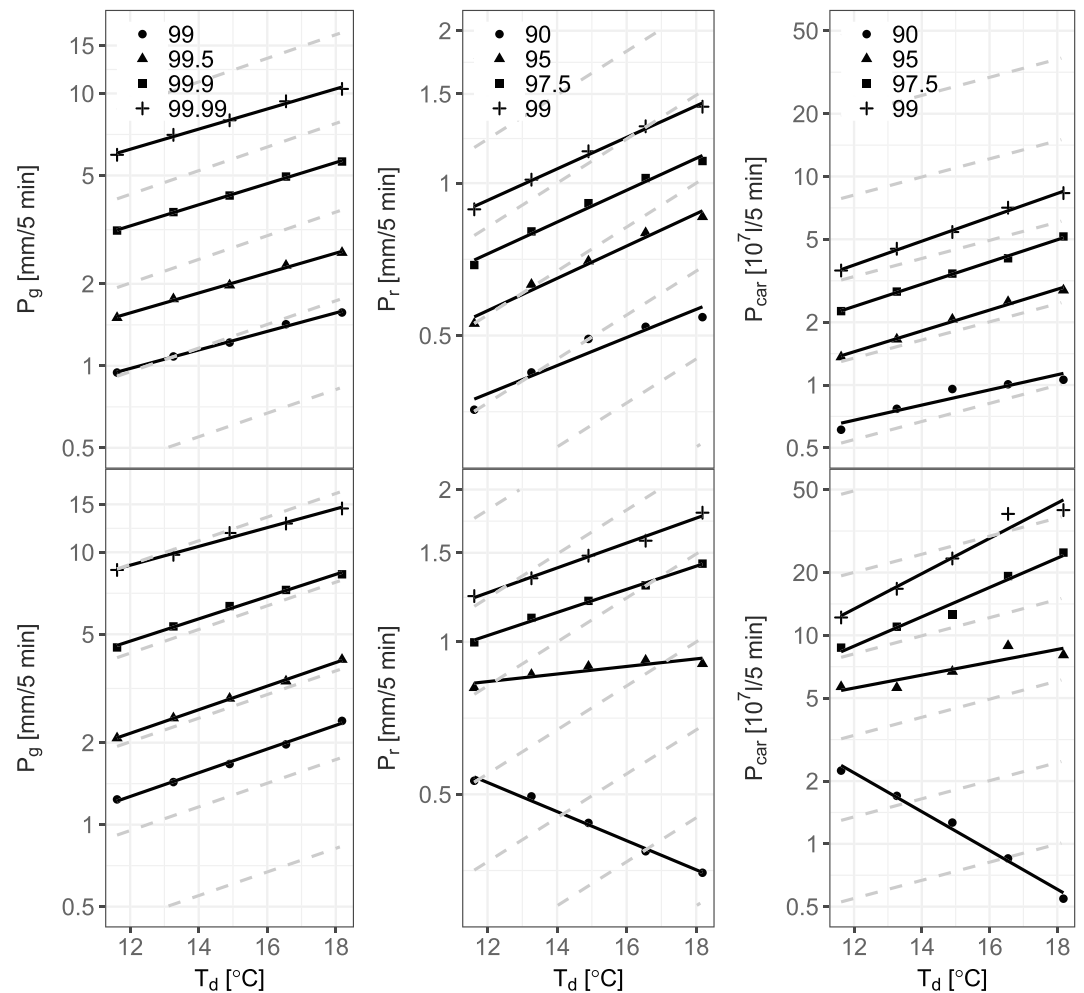
Figure 7. Scaling of high percentiles of various rainfall measures with dew point temperature T_d. (from left to right) Grid point intensities P_g, rain cell average intensities P_r, and cell-aggregated rain rate P_{car}. Upper panels show the results for phase I and lower panels for phase II. Percentiles for P_g are derived from all available data. That includes grid points with no precipitation. Each run is located on the x axis according to the average dew point temperature (lowest model level) of the whole model run. The CTRL simulation is at approximately 15 °C. Dashed lines indicate a fractional increase of 10%/K. Note the logarithmic y axes.

the presence of considerably larger rain cells in phase II. The fact that warmer runs generally have larger rain cells induces that scaling rates are higher than for grid point based or rain cell average intensities. In phase I, the cell-aggregated rain rate increases on average by 11.3%/K with a maximum of about 13.2%/K. In phase II, scaling rates reach 16.2%/K to almost 20%/K (97.5th and 99th percentiles). For the lower two percentiles in phase II, we observe as in the analysis for the rain cell average intensity that the scaling rates stall or even change sign.

These results highlight that the reshaping of the precipitation field between phases I and II has systematic consequences. Rain cells in phase I do not only grow substantially in size during the transition to phase II, they also become stronger in intensity. Both factors together yield higher precipitation amounts in phase II. Warmer temperatures and higher moisture availability amplify these two processes.

To visualize how cell size relates to cell intensity and cell-aggregated rain rate, we conditioned these statistics on the cell size (see equations (8) and (9)). The mean cell intensity increases with cell size (Figure 8). Also, the warmer runs have higher intensities for cells of the same size. The behavior can been seen for both phases. In phase II, however, up to cell sizes of 8 km, the intensity of all experiments is similar and, therefore, does not depend on dew point. This is about the same cell-size threshold as in Figure 5, where a decrease in cell number with warming turns into an increase.
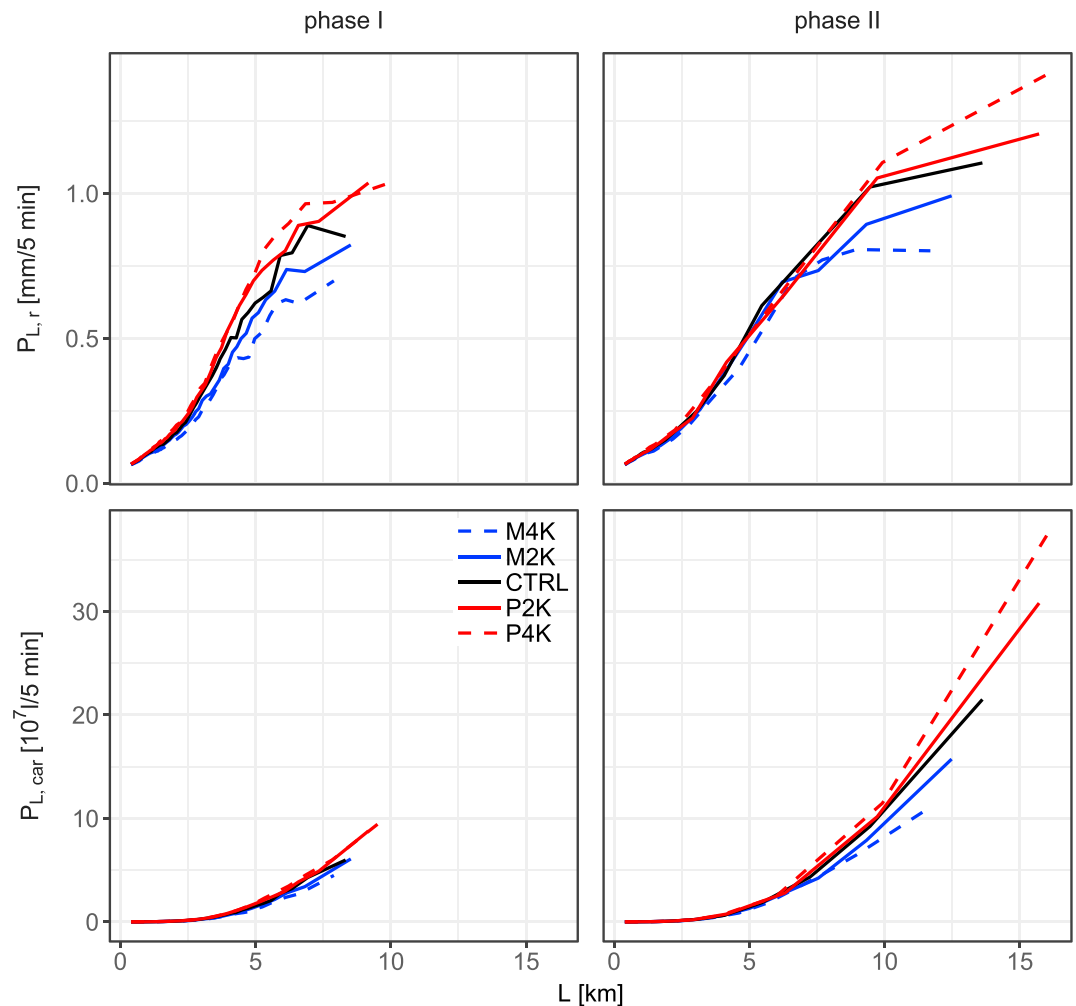
Figure 8. Average cell mean intensity conditional on cell size $P_{L,r}$ (upper panels) and cell-aggregated rate $P_{L,\text{car}}$ (lower panels). Cells are binned based on their size with (at least) 1,000 cells in each bin. The mean intensity and mean cell-aggregated rate are plotted against the mean cell size in each bin.

The cell-aggregated rain rate shows a similar behavior. Values mostly increase with warming. For instance, a rain cell in the P4K run has a larger aggregated rain rate than a rain cell of the same size in the M4K experiment. However, compared to the mean cell intensity, the relative difference of the maxima between the two phases is larger. Additionally, cell-aggregated rain rates, especially in phase II, steeply increase for the largest rain-cell sizes. Analogous to the mean cell intensity, the cell-aggregated rate is similar in all experiments up to a cell size of 8 km. This possibly explains the stagnation of scaling rates for the lower two percentiles of rain cell average intensity and cell-aggregated rain rate in Figure 7 since smaller rain cells have generally lower intensities.

In summary, warmer and moister atmospheric conditions lead to a faster growth of larger cells that are more intense. Together, they produce much higher cell-aggregated rain rates, well exceeding the CC rate of 7%/K.

Up to now, we only considered the cell mean intensity and did not investigate whether there is a redistribution of intensities within the cell. To investigate this, we made spatial composites of the 5,000 strongest precipitating cells during phase I (Figure 9), noting that a similar analysis for phase II is not possible due to the asymmetric shape of cells and their limited number. The composites show that rain cells cover, on average, a larger area in the P4K experiment than in the CTRL or M4K runs. Intensity increases as well. The corresponding radial averages extend our knowledge about their characteristic by the fact that intensities also increase at larger distances from the center. There is no indication of a redistribution of intensities toward the cell center at the expense of the intensities at the cell borders.
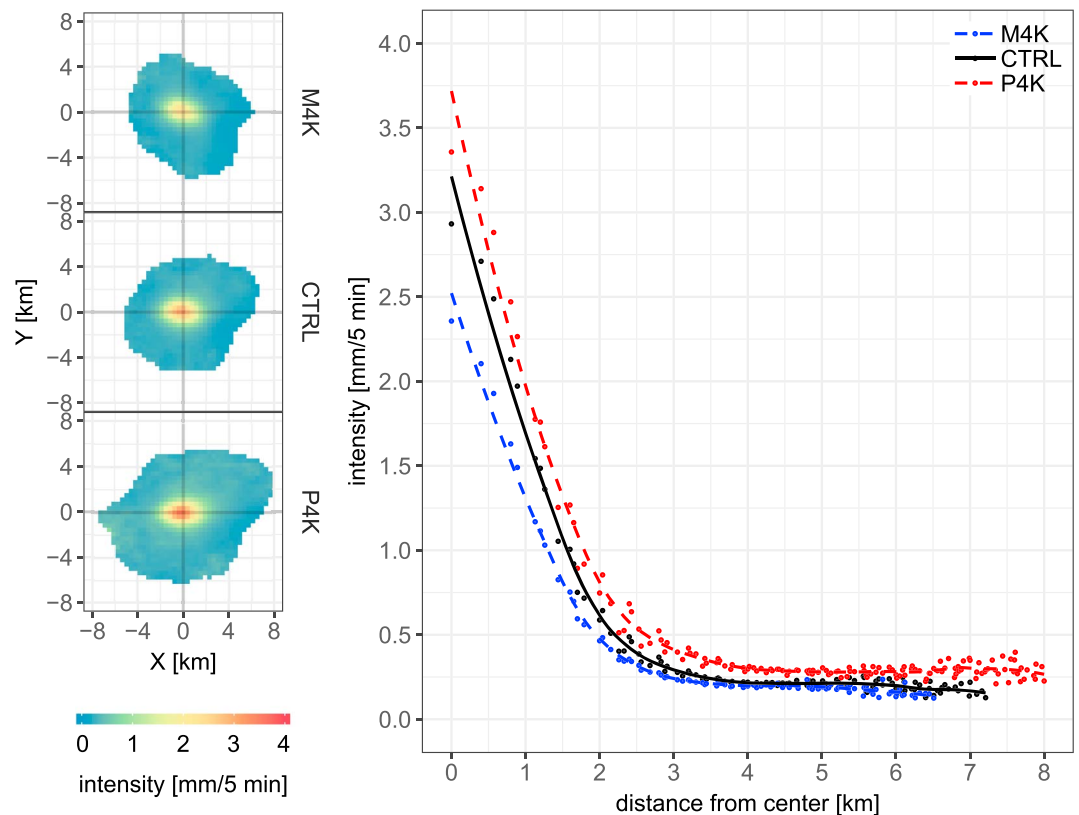
Figure 9. Composites (median) of the 5,000 strongest precipitating rain cells in phase I (left) and the corresponding radial averages (right). Rain cells are centered on the intensity weighted center of mass. Note that individual cells might be larger since we exclude grid points from the composite which are covered by less than 250 rain cells. Radial averages are constructed by using the number of cells that cover individual grid points of the same distance as weights. Dots in the right panel represent the calculated average intensity at a certain distance. The lines are local polynomial regression fits.

4. Conclusions and Discussion

This paper presents the results of idealized convection resolving simulations with a setup that comprises typical conditions for heavy rainfall in midlatitudes. The construction of the case was accomplished by compositing the forcing from a reanalysis product using a set of observed extremes (Lenderink et al., 2017) for the Netherlands following the approach of Loriaux et al. (2017). This produces a realistic forcing in terms of large-scale and surface-driven components. However, the fact that the meso-organization of the rain events takes longer forced us to stretch out the day from 24 to 36 hr in order to obtain a realistic timing in the peak of the convective activity as compared to the large-scale forcing. While this obviously reduces the realism of the case setup, the length of strong and organized convection in the period we study (less than 10 hr, phases I and II) is still within the lifespan of observed mesoscale convective systems (Feng et al., 2012). Another potential drawback is that our simulations make use of a rather simple microphysics scheme. A single-moment microphysics parameterization keeps the computational cost of our simulations on a feasible level. However, we note that the choice of the microphysics scheme can influence, for example, in-cloud properties such as updraft velocities and latent heating, mostly through ice-related processes (Fan et al., 2017). Moreover, the representation of ice-related microphysics can affect the simulated response of extreme precipitation to surface warming (Singh & O'Gorman, 2014).

Besides the control simulation, we conducted a set of experiments with perturbed initial temperature and specific humidity profiles. With this as a basis, we examined the evolution of the precipitation field throughout one diurnal cycle and its response to changes in atmospheric temperature and moisture content.

The simulations are characterized by a development toward larger rainfall structures in time. After the onset of precipitation, many small, regularly scattered rain cells are present (phase I). Correspondingly, the

precipitation area fraction quickly peaks. About 5 hr later (phase II), we observe that, while the precipitation area fraction has decreased, the precipitation field reshaped to fewer but larger rain cells. The distribution of rain cell size undergoes radical changes during the transition between the two phases. Many of the small cells of phase I decay, and fewer but much larger rain cells start to develop. At the same time, these larger rainfall structures have higher intensities than the small cells of phase I. Overall, precipitation rates, with minor fluctuations, continuously increase until the end of phase II.

Both phases demonstrate a systematic response to the initial conditions, but after the end of phase II, results are much more similar across all experiments. In both phases, rainfall rates are higher under warmer conditions and the dependency of extreme precipitation rates on surface dew point temperature exceeds the CC relation. However, cell mean intensities scale below the CC relation. These apparently conflicting rates are caused by the presence of more larger cells with higher intensities in the warmer simulations. Particularly in phase II, the cell size distribution is strongly determined by the largest rain cells. Even more, the growth of the largest rain cells with higher temperatures occurs at the cost of smaller sized rain cells. Consequently, the number of rain cells decreases. A conditional analysis of cell intensity on its size revealed a strong relation between the two characteristics. Indeed, area and mean intensity combined as the cell-aggregated rain rate shows a much stronger scaling with ambient dew point temperature, well exceeding the CC relation in both phases. The increase of intensities throughout most of the rain cell area plays a key role in this context.

Our results suggest that higher temperatures and a proportional increase of moisture availability according to the CC relation lead to a stronger organization of convective precipitation cells to larger spatial extent with higher intensities. We find no signal of a concentration or limitation of intensity increase to the center of rain cells accompanied by a decrease of the spatial extent and a redistribution of moisture as proposed by Wasko et al. (2016), Li et al. (2018), and Peleg et al. (2018). We note that these studies cover different regions of the world with different climates which complicates a comparison. In this context moisture limitation may play an important role for the redistribution of intensities within rain cells. Also, besides technical aspects (e.g., different metrics for the spatial extent or the use of dew point versus dry bulb temperature), part of the conflicting results may be explained by the approach to define rain events. For instance, Wasko et al. (2016) and Li et al. (2018) cluster station observations with simultaneous rain within a certain radius to rainfall events. This method considers only larger storms and misses information at locations without stations. Here we include finer details of convective rain cells and are able to sample a more continuous spectrum of the their size in the range from around 12 to 18 °C dew point temperature. Given this, we find that intensity and size of rain cells jointly increase under warming atmospheric conditions which is in line with the results of Lochbihler et al. (2017) and Lenderink et al. (2017).

References

Allen, M. R., & Ingram, W. J. (2002). Constraints on future changes in climate and the hydrologic cycle. *Nature*, *419*(6903), 224–232. https://doi.org/10.1038/nature01092

Attema, J., Loriaux, J., & Lenderink, G. (2014). Extreme precipitation response to climate perturbations in an atmospheric mesoscale model. *Environmental Research Letters*, *9*(1), 14003. https://doi.org/10.1088/1748-9326/9/1/014003

Berg, P., Moseley, C., & Haerter, J. O. (2013). Strong increase in convective precipitation in response to higher temperatures. *Nature Geoscience*, *6*, 181–185. https://doi.org/10.1038/ngeo1731

Böing, S. J., Jonker, H. J. J., Siebesma, A. P., & Grabowski, W. W. (2012). Influence of the subcloud layer on the development of a deep convective ensemble. *Journal of the Atmospheric Sciences*, *69*(9), 2682–2698. https://doi.org/10.1175/JAS-D-11-0317.1

Dee, D. P., Uppala, S. M., Simmons, A. J., Berrisford, P., Poli, P., Kobayashi, S., & Vitart, F. (2011). The ERA-Interim reanalysis: Configuration and performance of the data assimilation system. *Quarterly Journal of the Royal Meteorological Society*, *137*(656), 5530–597. https://doi.org/10.1002/qj.828

Fan, J., Han, B., Varble, A., Morrison, H., North, K., Kollias, P., & Wang, Y. (2017). Cloud-resolving model intercomparison of an MC3E squall line case: Part I. Convective updrafts. *Journal of Geophysical Research: Atmospheres*, *122*, 9351–9378. https://doi.org/10.1002/2017JD026622

Feng, Z., Dong, X., Xi, B., McFarlane, S. A., Kennedy, A., Lin, B., & Minnis, P. (2012). Life cycle of midlatitude deep convective systems in a Lagrangian framework. *Journal of Geophysical Research*, *117*, D23201. https://doi.org/10.1029/2012JD018362

Fischer, E. M., & Knutti, R. (2016). Observed heavy precipitation increase confirms theory and early models. *Nature Climate Change*, *6*(11), 986–991. https://doi.org/10.1038/nclimate3110

Grabowski, W. W. (1998). Toward cloud resolving modeling of large-scale tropical circulations: A simple cloud microphysics parameterization. *Journal of the Atmospheric Sciences*, *55*(21), 3283–3298. https://doi.org/10.1175/1520-0469(1998)055<3283:TCRMOL>2.0.CO;2

Haerter, J. O., Berg, P., & Moseley, C. (2017). Precipitation onset as the temporal reference in convective self-organization. *Geophysical Research Letters*, *44*, 6450–6459. https://doi.org/10.1002/2017GL073342

Heus, T., van Heerwaarden, C. C., Jonker, H. J. J., Pier Siebesma, A., Axelsen, S., van den Dries, K., & Vilà-Guerau de Arellano, J. (2010). Formulation of the Dutch Atmospheric Large-Eddy Simulation (DALES) and overview of its applications. *Geoscientific Model Development*, *3*(2), 415–444. https://doi.org/10.5194/gmd-3-415-2010

Lenderink, G., Barbero, R., Loriaux, J. M., & Fowler, H. J. (2017). Super-Clausius-Clapeyron scaling of extreme hourly convective precipitation and its relation to large-scale atmospheric conditions. *Journal of Climate*, *30*(15), 6037–6052. https://doi.org/10.1175/JCLI-D-16-0808.1

Lenderink, G., Barbero, R., Westra, S., & Fowler, H. J. (2018). Reply to comments on "Temperature-extreme precipitation scaling: A two-way causality?" *International Journal of Climatology*, *38*(12), 4664–4666. https://doi.org/10.1002/joc.5799

Lenderink, G., Mok, H. Y., Lee, T. C., & Van Oldenborgh, G. J. (2011). Scaling and trends of hourly precipitation extremes in two different climate zones—Hong Kong and the Netherlands. *Hydrology and Earth System Sciences*, *15*(9), 3033–3041. https://doi.org/10.5194/hessd-8-4701-2011

Lenderink, G., & van Meijgaard, E. (2008). Increase in hourly precipitation extremes beyond expectations from temperature changes. *Nature Geoscience*, *1*(8), 511–514. https://doi.org/10.1038/ngeo262

Li, J., Wasko, C., Johnson, F., Evans, J. P., & Sharma, A. (2018). Can regional climate modeling capture the observed changes in spatial organization of extreme storms at higher temperatures? *Geophysical Research Letters*, *45*, 4475–4484. https://doi.org/10.1029/2018GL077716

Lochbihler, K., Lenderink, G., & Siebesma, A. P. (2017). The spatial extent of rainfall events and its relation to precipitation scaling. *Geophysical Research Letters*, *44*, 8629–8636. https://doi.org/10.1002/2017GL074857

Loriaux, J. M., Lenderink, G., Roode, S. R. D., & Siebesma, A. P. (2013). Understanding convective extreme precipitation scaling using observations and an entraining plume model. *Journal of the Atmospheric Sciences*, *70*(11), 3641–3655. https://doi.org/10.1175/JAS-D-12-0317.1

Loriaux, J. M., Lenderink, G., & Siebesma, A. P. (2017). Large-scale controls on extreme precipitation. *Journal of Climate*, *30*(3), 955–968. https://doi.org/10.1175/JCLI-D-16-0381.1

Meijgaard, E. v., Ulft, L. H. v., Lenderink, G., Roode, S. R. d., Wipfler, E. L., Boers, R., & Timmermans, R. M. A. v. (2012). *Refinement and application of a regional atmospheric model for climate scenario calculations of Western Europe*. Wageningen: Royal Netherlands Meteorological Institute.

Mishra, V., Wallace, J. M., & Lettenmaier, D. P. (2012). Relationship between hourly extreme precipitation and local air temperature in the United States. *Geophysical Research Letters*, *39*, L16403. https://doi.org/10.1029/2012GL052790

Moseley, C., Berg, P., & Haerter, J. O. (2013). Probing the precipitation life cycle by iterative rain cell tracking. *Journal of Geophysical Research: Atmospheres*, *118*, 13,361–13,370. https://doi.org/10.1002/2013JD020868

Moseley, C., Hohenegger, C., Berg, P., & Haerter, J. O. (2016). Intensification of convective extremes driven by cloud-cloud interaction. *Nature Geoscience*, *9*(10), 748–752. https://doi.org/10.1038/ngeo2789

Muller, C. J., O'Gorman, P. A., & Back, L. E. (2011). Intensification of precipitation extremes with warming in a cloud-resolving model. *Journal of Climate*, *24*(11), 2784–2800. https://doi.org/10.1175/2011JCLI3876.1

Pall, P., Allen, M. R., & Stone, D. A. (2007). Testing the Clausius–Clapeyron constraint on changes in extreme precipitation under CO_2 warming. *Climate Dynamics*, *28*(4), 351–363. https://doi.org/10.1007/s00382-006-0180-2

Peleg, N., Marra, F., Fatichi, S., Molnar, P., Morin, E., Sharma, A., & Burlando, P. (2018). Intensification of convective rain cells at warmer temperatures observed from high-resolution weather radar data. *Journal of Hydrometeorology*, *19*(4), 715–726. https://doi.org/10.1175/JHM-D-17-0158.1

Pfahl, S., O'Gorman, P. A., & Fischer, E. M. (2017). Understanding the regional pattern of projected future changes in extreme precipitation. *Nature Climate Change*, *7*(6), 423–427. https://doi.org/10.1038/nclimate3287

Prein, A. F., Liu, C., Ikeda, K., Trier, S. B., Rasmussen, R. M., Holland, G. J., & Clark, M. P. (2017). Increased rainfall volume from future convective storms in the US. *Nature Climate Change*, *7*(12), 880–884. https://doi.org/10.1038/s41558-017-0007-7

Romps, D. M. (2011). Response of tropical precipitation to global warming. *Journal of the Atmospheric Sciences*, *68*(1), 123–138. https://doi.org/10.1175/2010JAS3542.1

Singh, M. S., & O'Gorman, P. A. (2014). Influence of microphysics on the scaling of precipitation extremes with temperature. *Geophysical Research Letters*, *41*, 6037–6044. https://doi.org/10.1002/2014GL061222

Singleton, A., & Toumi, R. (2013). Super-Clausius-Clapeyron scaling of rainfall in a model squall line. *Quarterly Journal of the Royal Meteorological Society*, *139*(671), 334–339. https://doi.org/10.1002/qj.1919

Tebaldi, C., Hayhoe, K., Arblaster, J. M., & Meehl, G. A. (2006). Going to the extremes. *Climatic Change*, *79*(3), 185–211. https://doi.org/10.1007/s10584-006-9051-4

Trenberth, K. E., Dai, A., Rasmussen, R. M., & Parsons, D. B. (2003). The changing character of precipitation. *Bulletin of the American Meteorological Society*, *84*(9), 1205–1217. https://doi.org/10.1175/BAMS-84-9-1205

Wasko, C., Lu, W. T., & Mehrotra, R. (2018). Relationship of extreme precipitation, dry-bulb temperature, and dew point temperature across Australia. *Environmental Research Letters*, *13*(7), 74031. https://doi.org/10.1088/1748-9326/aad135

Wasko, C., Sharma, A., & Westra, S. (2016). Reduced spatial extent of extreme storms at higher temperatures. *Geophysical Research Letters*, *43*, 4026–4032. https://doi.org/10.1002/2016GL068509

Westra, S., Fowler, H. J., Evans, J. P., Alexander, L. V., Berg, P., Johnson, F., & Roberts, N. M. (2014). Future changes to the intensity and frequency of short-duration extreme rainfall. *Reviews of Geophysics*, *52*, 522–555. https://doi.org/10.1002/2014RG000464